A COMPARISON OF ANALYTICAL METHODS

DRAG COEFFICIENT OF A CYLINDER

Giancarlo Bruschi   Tomoko Nishioka

Kevin Tsang   Rick Wang

March 21, 2003

MAE 171A

Friday PM3

Abstract

In this experiment, the drag coefficient of a cylinder was calculated from data obtained by performing tests in a water tunnel at three different flow velocities. Two methods of analysis were used to calculate drag measurements on the cylinder: a control surface over the cylinder and a control volume over the test section. In the control surface method, pressure distribution data was gathered by pressure probes on the cylinder. In contrast, the control volume analysis was carried out by measuring velocities in the test section by a Laser-Doppler Velocimeter (LDV). A comparison was then made between the results and error obtained by the two methods of analysis and data acquisition. From the pressure data, the drag coefficient was found to be 1.21, 1.21, and 1.18 at the respective velocities of 0.9, 1.4, 1.75 m/s. In comparison, the velocity measurements at 16 cylinder diameters downstream, yielded a drag coefficient of 1.06, 1.34, and 1.24 respectively. The cause and implications of the discrepancy between the two methods are discussed in this report.

Contents

List of Figures

List of Tables

1 Introduction

1.1 Applications of Fluid Dynamics

Understanding the drag characteristics of objects in fluid flow is essential for engineering design aspects, such as to reduce the drag on automobiles, aircrafts, and buildings. The phenomenon of drag can be simulated and measured by recreating water flow over an object. Theories such as conservation of momentum and continuity may be combined with experimental data to study the behavior of fluid flow around an object.

1.2 Flow Over A Cylinder

In this experiment, a water tunnel is used to analyze the effects of fluid flow over a cylinder. As the water circulates through the closed-loop system, the cylinder obstructs the path of the fluid flow causing the water to deviate from its otherwise uninterrupted flow path. The uniform velocity profile of the flow becomes non-uniform as the fluid passes by the cylinder. The drag caused by the cylinder can be calculated through two different methods: control surface analysis consisting of pressure measurements around the cylinder, and control volume analysis consisting of velocity measurements taken before and after the cylinder. These experimentally obtained pressure and velocity measurements provide the necessary data required to find the coefficient of drag of the cylinder for this experiment. The equations used to calculate the drag coefficient is described in detail in the procedure and theory. With these two methods of obtaining the drag coefficient, the fluid flow around the cylinder can be observed, analyzed, and compared.

2 Theory

2.1 Fluid Mechanics Terminology

Drag is the component of a force acting on a body that is projected along the direction of motion. Both shear forces and pressure induce drag on a body in motion. Shear forces, known as *skin friction drag*, are more significant in streamlined objects, while the *pressure drag* is more significant in blunt objects [5]. Fig. (1) shows the net drag force acting on a cylinder.

The drag force is often non-dimensionalized as a function of Reynolds number. This is then referred to as the *drag coefficient* (eq. 1). Similarly, the pressure acting on each differential element of an object may be normalized by the dynamic freestream pressure $\frac{1}{2}\rho U_\infty^2$ to obtain the *pressure coefficient* (eq. 2). This quantity may also be rewritten as the reduced pressure coefficient (eq. 3).

$$C_D = \frac{F_D}{\frac{1}{2}\rho U^2 A} \tag{1}$$

$$C_p = \frac{\Delta p}{\frac{1}{2}\rho U^2} \tag{2}$$

$$C_p = \frac{q}{q_\infty} \tag{3}$$

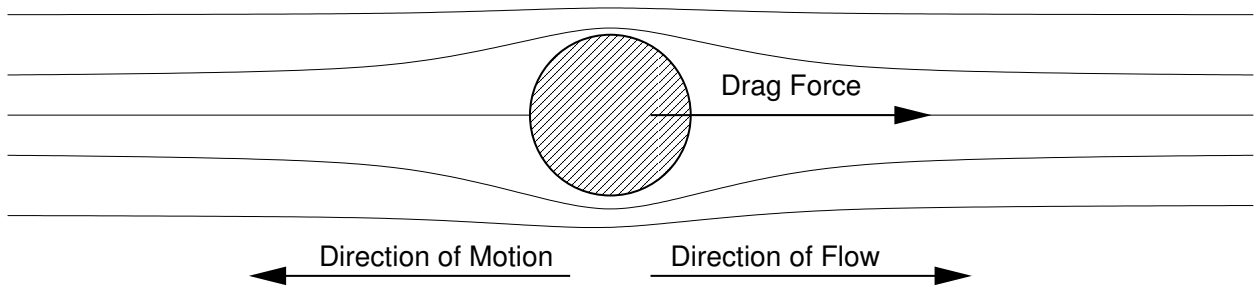

Figure 1: Drag force on a cylinder.

2.2 Flow Considerations

For low Reynolds numbers, when $Re < 3 \cdot 10^5$, viscous forces are predominant and the flow may be generally considered laminar [6]. In this experiment, the largest Reynolds number used was $Re \approx 5 \cdot 10^4$, which is well below the transition to turbulent flow. However, while the flow over the forward portion of the cylinder is laminar, the wake is known to be highly turbulent due to the boundary layer separation [5]. For laminar flow conditions, the boundary layer separation occurs at approximately 82 degrees from the stagnation point [4]. After this point, the pressure coefficient remains negative and approaches -1.00 (fig. 2) [1]. This increases the severity of the pressure gradient and increases total pressure drag. Data taken downstream from the cylinder must then be considered with the effects of the turbulent wake.

Other considerations such as compressibility, surface roughness, vortices, thermal effects, gravity, and boundary layer development may be neglected for the purpose of this experiment. Compressibility effects are known to be ngligible for liquids due to a large bulk modulus E_v. The cylinder tested is smooth and the flow remains defined by the Reynolds number. The boundary layer over the test section walls were assumed to be small relative to the width of the test section and are taken into account in the analysis. Turbulent effects are not considered in calculations, but are considered in the discussion and the results.

2.3 Control Surface Method

One method of calculating the drag coefficient of the cylinder is to approximate the total drag associated with the pressure drag. The pressure drag is calculated from the pressure distribution over the control surface. This method provides a suitable estimate since the total drag on the cylinder is mostly due to the pressure drag.

2.3.1 Pressure Distribution Analysis

The total pressure drag on the cylinder is calculated by integrating the differential pressure components over the surface of the cylinder (eq. 4) [3]. The control surface over the
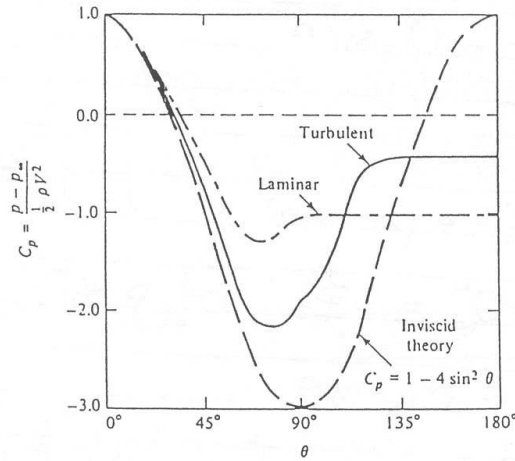
Figure 2: Pressure coefficients over cylinder.

cylinder is shown in fig. (3). Each differential pressure component p acts in the opposite direction of the surface normal and must be projected along the direction of travel to obtain its contribution to total pressure drag.

$$F_{D,p} = \iint_S p(\theta) \cos\theta \, \mathrm{d}a \tag{4}$$

In this equation, p represents the gage pressure and θ represents the angle between the drag direction and the surface normal. These values are a function of position and must be integrated over the surface area to obtain the net pressure drag force, $F_{D,p}$.
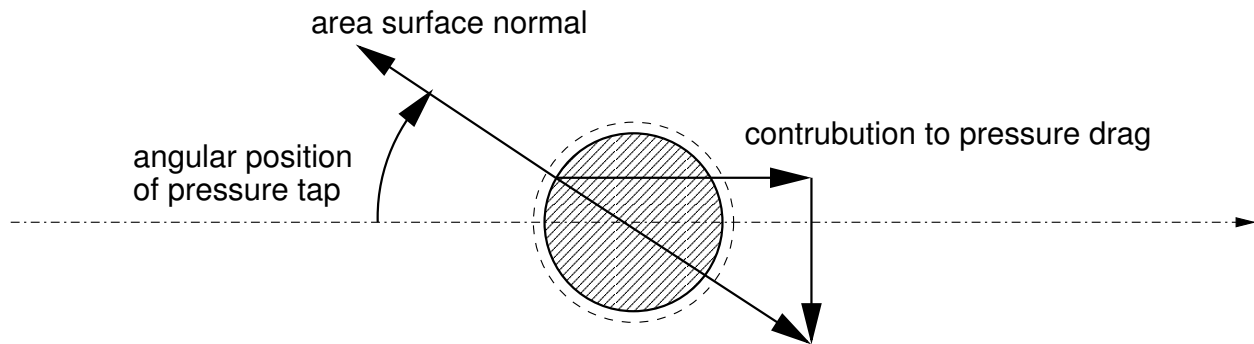
Figure 3: Control surface over cylinder cross–section.

By making the approximation that $F_D \approx F_{D,p}$, eq. (4) may be substituted into the the expression for drag coefficient (eq. 1). In the resulting equation, the dynamic pressure term may be moved inside the integral and combined with the local gage pressure p to obtain the pressure coefficient (eq. 2). The drag coefficient may then be rewritten as eq. (5) [3].

$$C_D \approx C_{D,p} = \frac{\iint_S C_p \cos\theta \, \mathrm{d}a}{A} \tag{5}$$

In eq. (5), A is the cross sectional area because the cylinder may be considered a blunt object. The integral in eq. (5) may also be rewritten in terms of θ by the substituting the differential area element with the arc length times the unit depth ($\mathrm{d}a = (D/2)b\mathrm{d}\theta$). The term C_p may be expanded via eq. (2). After doing so, the terms length b and diameter D may be cancelled. Since the flow is symmetric over both the top and bottom of the cylinder, the integral may be re-defined, and the $1/2$ term cancels as well to yield eq. (6).

$$C_D \approx \int_0^\pi C_p \cos\theta \, \mathrm{d}\theta \tag{6}$$

However, continuous pressure data cannot be easily gathered over a given area. Instead, pressure probes are used to gather pressure data at given points. To adapt the continuous equation for discrete data points, an integral approximation method such as the trapezoidal rule must be used (eq. 7), where $C_{D,i}$ is defined by eq. (8).

$$C_D \approx \sum_{i=1}^N \frac{(C_{D,i+1} + C_{D,i})(\theta_{i+1} - \theta_i)}{2} \tag{7}$$

$$C_{D,i} = C_{p,i} \cos\theta_i \tag{8}$$

In the case of inviscid flow, the pressure coefficients may be modeled by eq. (9) [2]. Integration by eq. (5) results in no drag as expected from the omission of viscous effects. The inviscid model serves as a basis of comparison for later calculations.

$$C_p = 1 - 4\sin^2\theta \tag{9}$$

2.3.2 Interpreting Pitot Tube Data

The pressure at each data point may be obtained from Bernoulli's equation (eq. 10) by rewriting it in terms of the manometer reading Δh (eq. 11). An expression for freestream velocity in the test section may be derived in terms of pressure measurements (eq. 12) from eq. (11). Bernoulli's equation is appropriate under the assumptions of incompressible, irrotational, and inviscid flow.

$$p_a - p_b = \frac{1}{2}\rho_\infty U_\infty{}^2 = q_\infty \tag{10}$$

$$p_a - p_b = \rho_1 \Delta h g \tag{11}$$

$$U_\infty = \left(\frac{2\rho_1 \Delta h g_e}{\rho_\infty}\right)^{1/2} \tag{12}$$

2.4 Control Volume Method

Another method of finding the drag coefficient is to consider a control volume over the test section (fig. 4). This approach seeks to indirectly solve for the drag force by evaluating the flow passing through the control volume. Conservation of momentum may be used to solve the drag force, which can then be used to solve the drag coefficient.
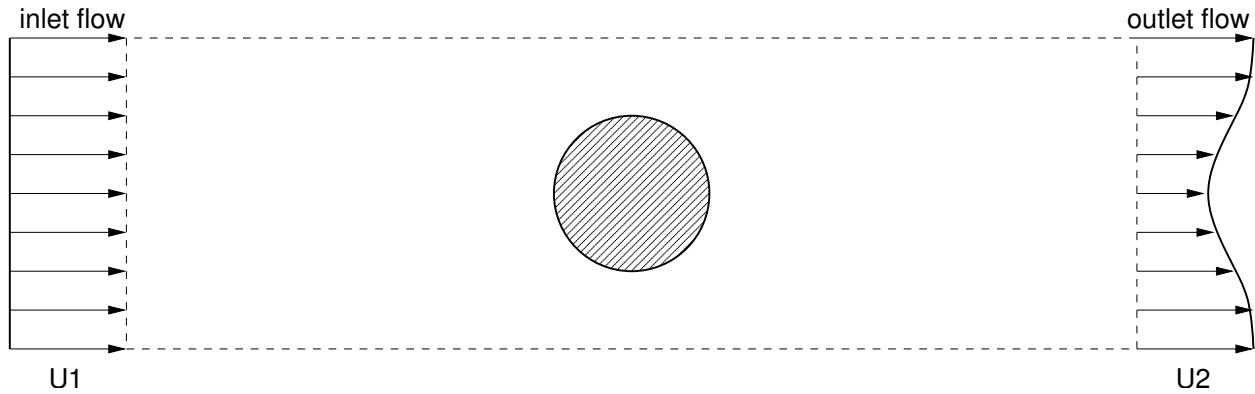

Figure 4: Control volume over the length of test section.

2.4.1 Conservation of Momentum

An expression for the drag force on a cylinder (eq. 13) may be obtained from the momentum loss of fluid passing through the control volume. The subscript 1 denotes the inlet of the control volume, and 2 denotes the outlet.

$$F_D = \iint_1 U_{1,\infty} \rho \vec{U}_1(y) \cdot \mathrm{d}\vec{a} + \iint_2 U_{2,\infty} \rho \vec{U}_2(y) \cdot \mathrm{d}\vec{a} \tag{13}$$

The expression for drag (eq. 13) may then be rewritten in terms of the velocity difference over the inlet and outlet to produce a single integrand. This was done by substituting the result from applying conservation of mass to the control volume (eq. 14). The displacement thickness Δ was approximated as zero, setting the upstream and downstream velocities to be equal. The integrand was then non-dimensionalized, and the limits of integration were redefined.

$$U_{1,\infty} = U_{2,\infty} \left(1 - \frac{\Delta}{h}\right) \tag{14}$$

$$\Delta \equiv \int_0^h \left(1 - \frac{U_2(y)}{U_{2,\infty}}\right) \mathrm{d}y \tag{15}$$

From the previous equations, an expression for drag per unit length of the cylinder, in terms of dynamic pressure $\frac{1}{2}\rho U^2$ and the normalized outlet velocity $U_2(y)/U_{2,\infty}$, may be derived (eq. 16) [3]. The continuous integral must then be approximated by a summation (eq. 17), where $F_{D,i}$ is given by eq. (18).

$$F_D = \frac{1}{2}\rho U_{1,\infty}^2 \int_0^h \frac{U_2(y)}{U_{2,\infty}} 2 \left[1 - \left(\frac{U_2(y)}{U_{2,\infty}}\right)\right] \mathrm{d}y \tag{16}$$

$$F_D \approx \frac{1}{2}\rho U_{1,\infty}^2 \sum_{i=1}^N \frac{(F_{D,i+1} + F_{D,i})(y_{i+1} - y_i)}{2} \tag{17}$$

$$F_{D,i} = \frac{U_2(y)_i}{U_{2,\infty,i}} 2 \left[1 - \left(\frac{U_2(y)_i}{U_{2,\infty,i}}\right)\right] \tag{18}$$

This value of drag force will include both the pressure drag and skin friction drag, but may also pick up drag from the test section walls as well. For this reason, it is important to choose a section h such that the boundary layer effects are negligible. The drag force (eq. 17) is non-dimensionalized as in eq. (1) to yield the drag coefficient.

2.4.2   Interpreting LDV Data

Velocity measurements obtained by the LDV are calculated from the frequency of scattered light due to particles flowing through a focal control volume (fig. 5). In the focal control volume, an interference pattern is formed where the two monochromatic laser beams cross. The fringe spacing Δ is expressed as a function of the laser wavelength λ and the angle between the beams Θ (eq. 19).

$$\Delta = \frac{\lambda}{2 \sin \frac{\Theta}{2}} \tag{19}$$

In this experiment, the spacing between the two lasers was 2.32 degrees and the wavelength of the blue light was 488 nm. The flow velocity U_x is then calculated from the fringe spacing Δ and frequency of modulation f by eq. (20).

$$f = \frac{U_x}{\Delta} = \frac{2U_x}{\lambda} \sin \frac{\Theta}{2} \tag{20}$$

Particles flowing through the interference pattern scatter a light signal that is collected by the LDV instrument. By traversing the focal control volume over the test section, various velocity profiles are obtained.
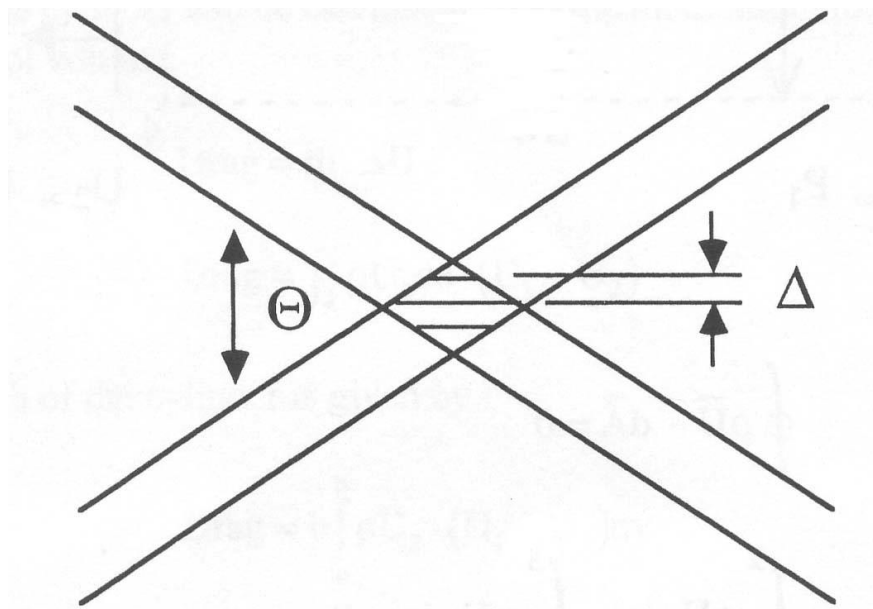
Figure 5: LDV focal volume.

3 Procedure

All experiments were conducted at the Mechanical Engineering Undergraduate Laboratory at the University of California, San Diego. The general setup consisted of a 1 in. diameter smooth cylinder in a closed-loop water tunnel system. The test section was a 1 ft. by 1 ft. acrylic enclosure. For the control surface method, measurements were taken from pitot tubes embedded in the cylinder. For the control volume method, an Aerometrics LDV system was configured to perform data acquisition along the test section volume.

3.1 Water Tunnel Velocity Calibration

The water tunnel was calibrated to find a relationship between water velocity and the motor impeller speed. A LabView program, *Cylinder Pressure Distribution VI*, was used to record pressure measurements from the pitot-static tube as well as the various data points around the cylinder. Pressure readings were taken at a motor frequency of 0 Hz, for the offset, and then from 15-40 Hz, in 5 Hz increments. Once all data was collected, the offset was subtracted from all readings and corrected values were tabulated. The free-stream velocity was then calculated from eq. (12).

A graph of velocity versus motor frequency is plotted and a trendline is fitted to the plot. The equation of this line was used to find the exact motor frequency for 0.9, 1.4, and 1.75 m/s freestream velocity.

3.2 Pressure Distribution

The *Cylinder Pressure Distribution VI* was used to collect pressure data at the four velocities stated earlier (0 offset, 0.9, 1.4, 1.75 m/s). The offset was then subtracted from all pressure measurements to take into account. The pressure measurements were taken at locations indicated in Table 1.

The pressure coefficient, C_p, was calculated from eq. (3). Theoretical values of C_p were then calculated using eq. (9), to be used for comparison against the measured values. The drag coefficient for each of the three measured pressure coefficient distributions was

Data Point	1	2	3	4	5	6	7	8	9	10	11	12	13
Angle (deg)	0	22.5	45	56	67	78	90	101	112	123	135	157.5	180

Table 1: Locations of pressure taps on cylinder.

then calculated by eq. (6). A verification of the calculations was performed by integration of the ideal C_p in eq. (9), which confirmed the expected value of zero.

3.3 LDV Measurements

With the intention to compare the measurements taken by the LDV system with the pressure data, the water tunnel was calibrated using the LDV to measure the water velocity upstream. The Aerometrics Data View 1-D LDV Acquisition program (version 0.99ga) was used to execute velocity measurement sequences. In each sequence, the same motor frequencies from the pressure calibration were used to set the water velocity to 0.9, 1.4, and 1.75 m/s, due to their proximity in value. Particles were introduced into the water to allow the LDV system to accurately analyze the flow velocity. For each velocities, the LDV measured mean velocity and RMS error of the velocity of the water in the axial direction at increments shown in Table 2.

For 0.9, 1.4, and 1.75 m/s, the LDV system was used to measure the velocity profiles transverse to the axis of the cylinder at 6 diameters upstream, as well as 8 and 16 diameters downstream of the cylinder. Each of these data acquisition sequences were assigned a program identification code (Table 3).

These commands were loaded into the Data View program to acquire velocity measurements along each path. Once all procedures are run for 0.9 m/s, the results were saved and the procedure was repeated for the remaining velocities. The drag coefficient,

	6 upstream–6 downstream	6 downstream–16 downstream
Increment (dia.)	1.0	2.0

Table 2: LDV axial test increments.

Data Collection Path	Program Number
Axial	30002
6 upstream	30003
8 downstream	30004
16 downstream	30005

Table 3: LDV program identification codes

C_D, was then obtained by eq. (1).

4 Results

4.1 Data from Pressure Distribution

The motor frequencies corresponding with the three velocities, 0.9, 1.4, 1.75 m/s, were found to be 19.11, 30.91, and 39.16 Hz, respectively. The pressure coefficients at each position around the cylinder was compared to the ideal flow in fig. (6). The drag coefficients were then calculated for each of the three measured pressure distributions are tabulated in Table 4.
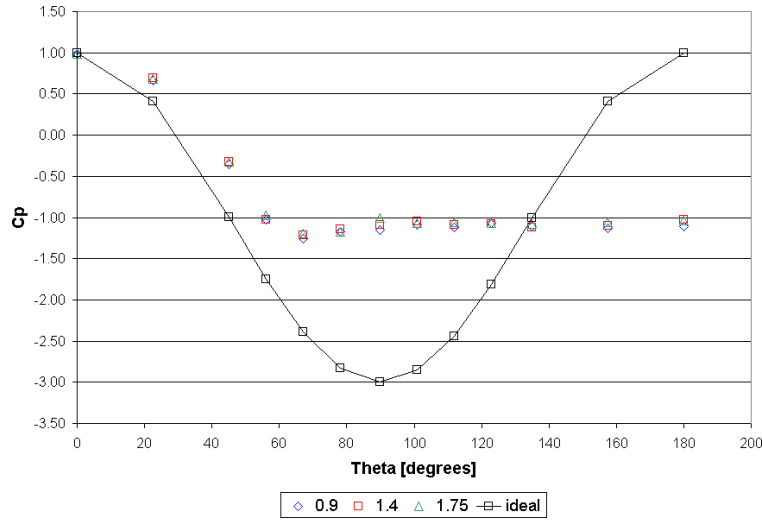
Figure 6: Pressure coefficients on cylinder.

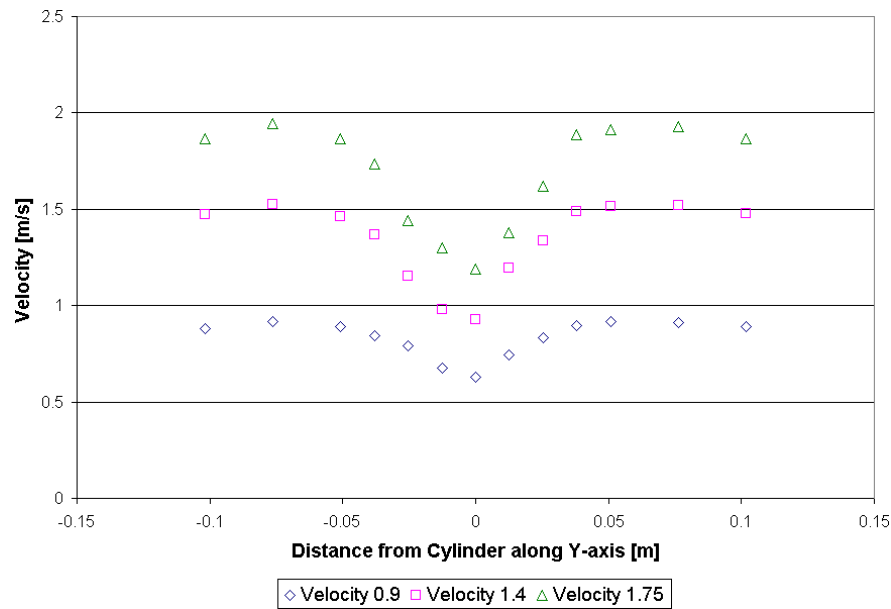| Flow Velocity $[m/s]$	C_D	Worst Error $[m/s]$	Random Error $[m/s]$
0.90	1.210	0.104	0.034
1.40	1.205	0.086	0.028
1.75	1.183	0.094	0.031

Table 4: Drag coefficients obtained from pressure data.

4.2 Data from LDV

The LDV experiment was run at the same motor frequencies used previously in the pressure distribution experiment. The mean velocity profiles at 8 diameters and 16 diameters downstream from the cylinder are shown in fig. (7). The RMS and normalized RMS, were recorded in fig. (13, 14).

The drag coefficient for each flow condition was calculated from the velocity measurements taken with the LDV system. These drag coefficient values for each velocity are tabulated in Table 5. The difference between these C_D values found with the LDV velocity measurements and those calculated from the pressure measurements will be reviewed later in the discussion . The ratios $\frac{U_{2,\infty}}{U_{1,\infty}}$ are tabulated in Table 6. These were compared to the theoretical values (eq. 14).

(a) 8 diameters downstream
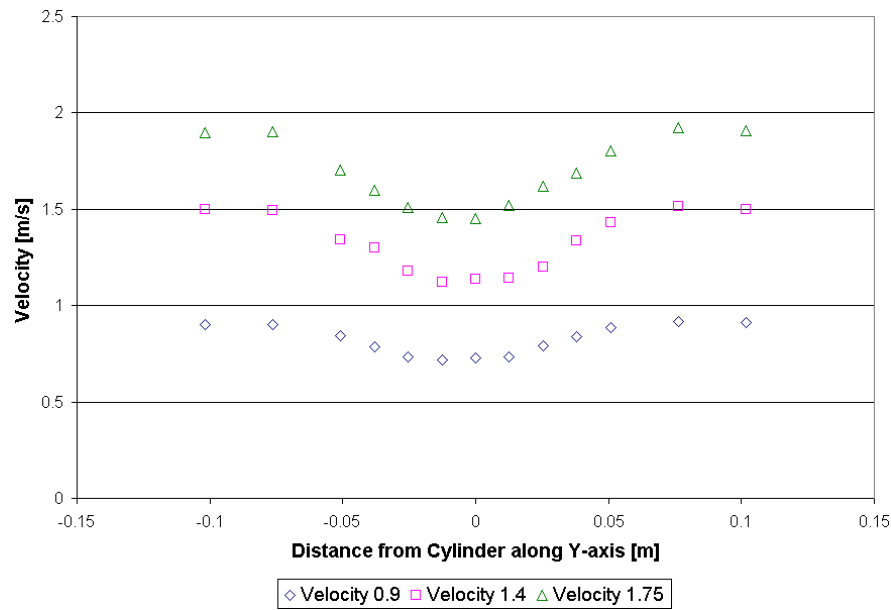
(b) 16 diameters downstream

Figure 7: Downstream velocity profiles.

Flow Velocity $[m/s]$	C_D	Worst Error $[m/s]$	Random Error $[m/s]$
0.90	0.91	0.95	0.33
1.40	1.11	0.41	0.15
1.75	1.18	0.31	0.11

(a) 8 diameters downstream

Flow Velocity $[m/s]$	C_D	Worst Error $[m/s]$	Random Error $[m/s]$
0.90	1.06	1.36	0.44
1.40	1.34	0.56	0.18
1.75	1.24	0.50	0.17

(b) 16 diameters downstream

Table 5: Drag coefficients obtained from LDV data.

Velocity $[m/s]$	$\frac{U_{2,\infty}}{U_{1,\infty}}$ 8D Downstream		$\frac{U_{2,\infty}}{U_{1,\infty}}$ 16D Downstream	
	measured	calculated	measured	calculated
0.90	1.07	1.05	1.06	1.06
1.40	1.09	1.07	1.08	1.08
1.75	1.08	1.07	1.06	1.08

Table 6: Comparison of downstream velocitiesi.

Re	C_D (pressure data)	C_D (LDV, 8D data)	C_D (LDV, 16D data)
26000	1.21	0.91	1.06
40000	1.20	1.11	1.34
50000	1.18	1.18	1.24

Table 7: Drag coefficients compared to Reynolds number.

5   Discussion

5.1   Calibration

The calibration data from the pressure distribution and LDV are compared in fig. (8). Both of the methods show highly agreeable relationships between the fluid velocity and the impeller motor frequency. However, the slope of the LDV method is slightly higher than the slope of the pressure distribution method. Despite the small difference, it seems that the calibration data of both the pressure distribution and the LDV may be reasonable exchanged.
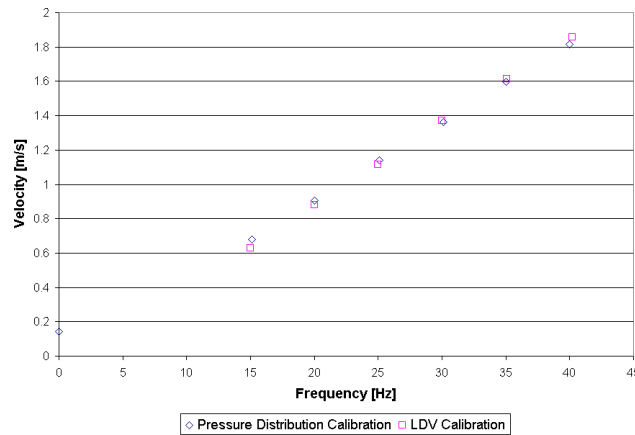

Figure 8: Comparison of calibration data.

5.2   Analysis of the Pressure Distribution Data

As seen in fig. (6), the experimental pressure distribution curve is consistent for all three velocities. This implies that within the velocity range used in this experiment, the pressure distribution around the cylinder is independent of the Reynolds number.

Fig. (6) shows that the calculated C_p curve for the three velocities deviate a great deal from the theoretical inviscid flow curve. As discussed in theory, for a cylinder in laminar flow, separation occurs at approximately 82 degreees from the stagnation point. It is evident that the experimental C_p values fluctuate slightly at a constant value of -1.00 after approximately 82 degrees. This suggests that after 82 degrees, the cylinder surface

is exposed to the turbulent wake due of the boundary layer separation as shown in fig. (2). The calculated C_D values were fairly consistent at approximately 1.2 over the range of Reynolds numbers tested (Table 4). These results exhibit strong agreement with the expected behavior shown in fig. (9).

5.3   Analysis of the LDV Data

As opposed to the coefficient of drag found in the control surface method, knowing the velocity throughout the control volume allows for the calculation of the drag coefficient by observing the momentum loss. Linear momentum theory requires that the sum of the time rate of change of the momentum plus the net outflow of momentum from the control volume must equal the drag force acting on the fluid in the control volume, eq. (13).

As seen in fig. (11), for all three velocities, the upstream velocity approaches zero as the fluid advances toward the cylinder surface. Behind the cylinder, velocity values reflect negative measurements. These negative velocity measurements are caused by the turbulent wake that exists due to the momentum deficiency in the fluid flow. The turbulent wake is formed by the low-pressure region due to the boundary layer separation. Thus, for the separated flow over the cylinder, there is a net unbalance of pressure forces in the direction of the flow, which results in the pressure drag.

At 6 diameters upstream, the velocity profile was fairly uniform as seen in fig. 12. However, further downstream, the velocity profile at the wall was not uniform (fig. 7). A comparison between the upstream and downstream velocity profiles suggests that the loss of momentum near the wall was due to viscous effects. This portion of the data was then omitted from the analysis.

Observation of the results of the C_D values obtained (Table 5) through the control volume method show that the error in the coefficient of drag calculated at 0.9 m/s is rather high. This unusually high error can be justified by looking at the collected data of the RMS profile at 6 diameters upstream in fig. (13(b)), where the data shows that the second to last data point of the RMS of 0.9 m/s velocity is unusually higher than
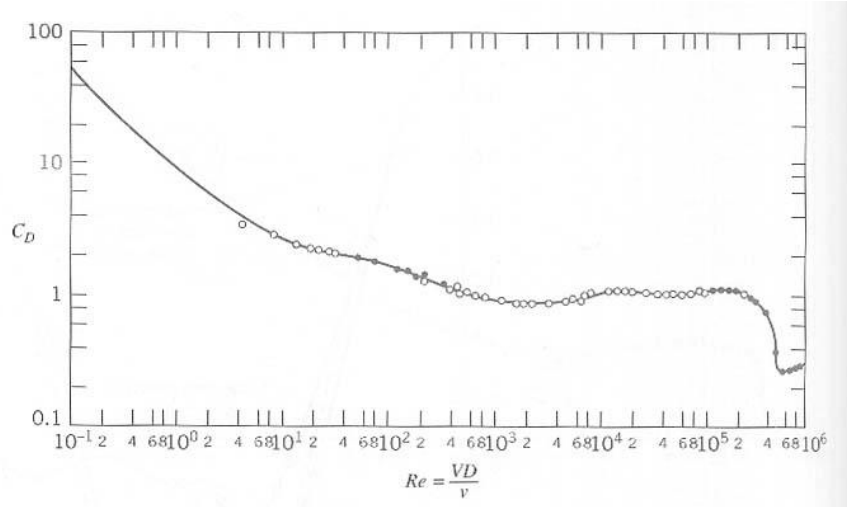
Figure 9: Variation of cylinder-drag coefficient with Reynolds number[1]

the rest of the data collected. Since the calculation of the coefficient of drag is directly influenced by the velocity at 6 diameters upstream, the unusually high error in C_D at 0.9 m/s can be justified.

5.4   Comparison of the Two Methods

In comparison to the drag coefficients obtained by the pitot pressure measurements, the C_D values that were calculated from the LDV generally resulted in slightly lower values as seen in Table 7, with the exception of the 1.75 m/s calculated by the LDV 16 diameters downstream data. Since the LDV method takes into consideration the entire control volume which includes the analysis on the wake, it would seem that the LDV method is more accurate calculating C_D compared to the pressure distribution method. However, in theory, it is explained that for a smooth cylinder under laminar flow, the coefficient of drag is independent of the velocity within the velocity range under analysis. Fig. (9) shows the coefficient of drag verses Reynolds number for a smooth circular cylinder. The Reynolds number used in this experiment lies between the values of 25600 and 49700, where in fig. (9), the drag coefficient is fairly constant.

In comparison of the resulting C_D values obtained from the two methods tabulated in

Table 7, it can be observed that the pressure distribution data results in a more constant value of C_D in comparison to the LDV method. Also, the LDV method results in higher error values compared to the pressure distribution method. These errors in the LDV method may be explained from the inaccuracy in the laser measurements instrument, perhaps due to the refraction of the laser beam at the acrylic walls, or also from the error associated with the three velocities that were controlled with the frequency obtained from the pressure distribution method.

6   Conclusion

In this experiment, the the drag coefficient of a cylinder was analyzed by considering the pressure distribution and the momentum loss in the wake. From the control surface method of analysis of the pressure distribution data, the drag coefficients were calculated to be 1.21±.03, 1.21±0.03, and 1.18±0.03 for the three flow velocities of 0.9, 1.4, and 1.75 m/s respectively. From the control volume analysis and LDV acquired velocity data 16 cylinder diameters downstream, the drag coefficients were 1.06±0.44, 1.34±0.18, and 1.24±0.17 at the same three velocities. Random error in the drag coefficient as determined from the control volume analysis ranged from 13% to 41%, while random error from the pressure measurements ranged from 2.3% to 2.8%. The larger error from the control volume analysis was primarily due to the large error from LDV measurements.

There was no significant difference in the drag coefficient over the different velocities tested, which indicates that the drag coefficient is fairly independent of Reynolds number in this range. This also implies that the drag coefficient may be more dependent on other factors, such as the object's shape. It is possible to conclude that coefficient of drag can be confirmed through various analytical methods such as those used in this experiment.

References

[1] J. D. Anderson, *Fundamentals of Aerodynamics*, 2nd ed.   McGraw-Hill, 1991, pp. 228–236.

[2] ——, *Fundamentals of Aerodynamics*, 2nd ed.   McGraw-Hill, 1991, section 3.13, pp. 195–200.

[3] R. J. Cattolica, "MAE171A/175A Mechanical Engineering Laboratory Manual," Winter quarter 2003, Experiment F2: Water Tunnel.

[4] ——, "MAE171A/175A Water Tunnel Lecture Notes," Winter quarter 2003.

[5] Fox and McDonald, *Introduction to Fluid Mechanics*, 5th ed.   John Wiley and Sons, Inc., 1998, section 9.7, pp. 444–457.

[6] ——, *Introduction to Fluid Mechanics*, 5th ed.   John Wiley and Sons, Inc., 1998, section 7.4, pp. 306–307.

A Calibration Data

y = 0.0424x + 0.0896
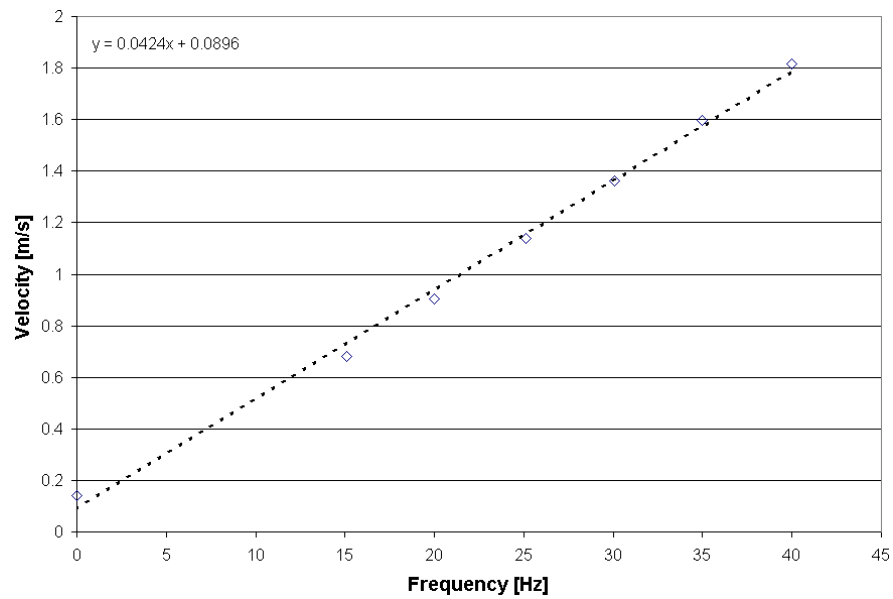
(a) Pressure Calibration Data

y = 0.0488x - 0.1003
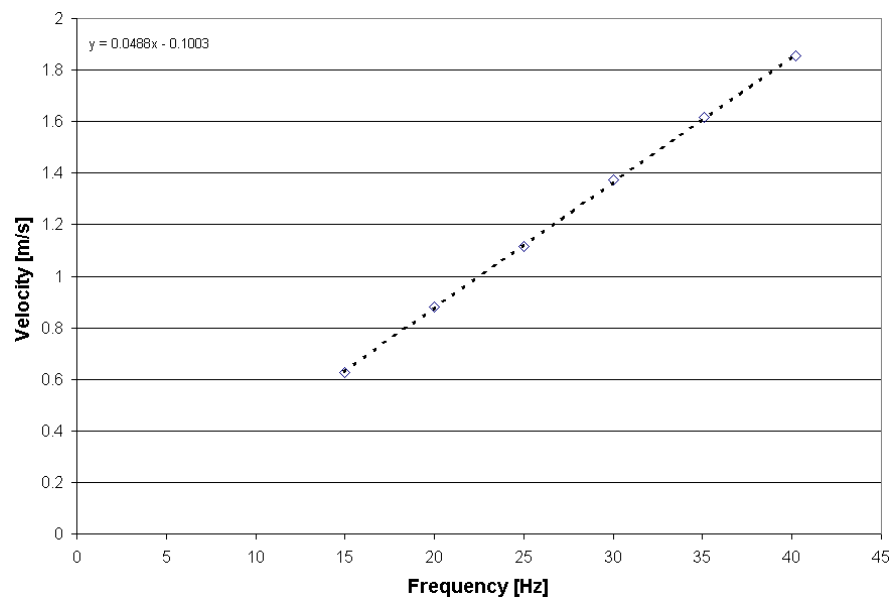
(b) LDV Calibration Data

Figure 10: Velocity and motor frequency correlation plots.
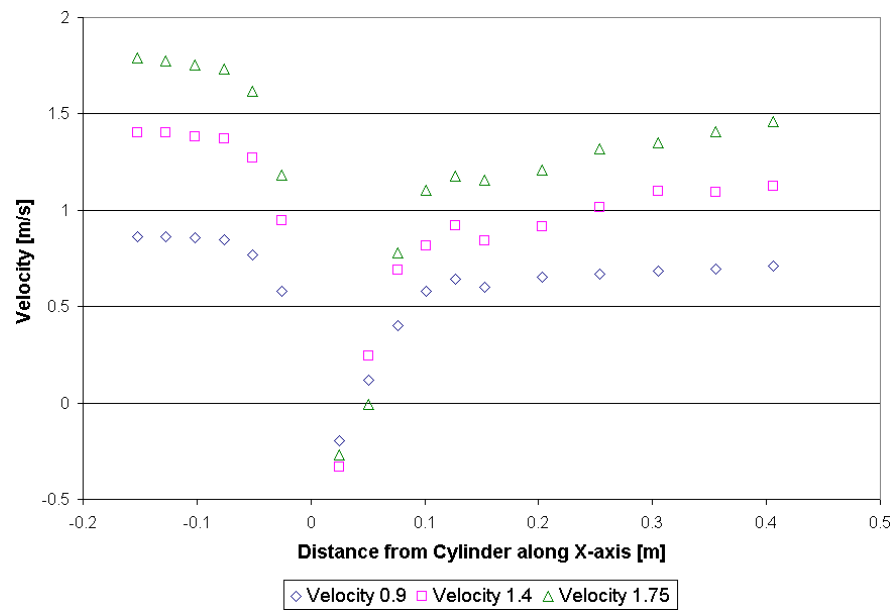
B   Supplemental Results
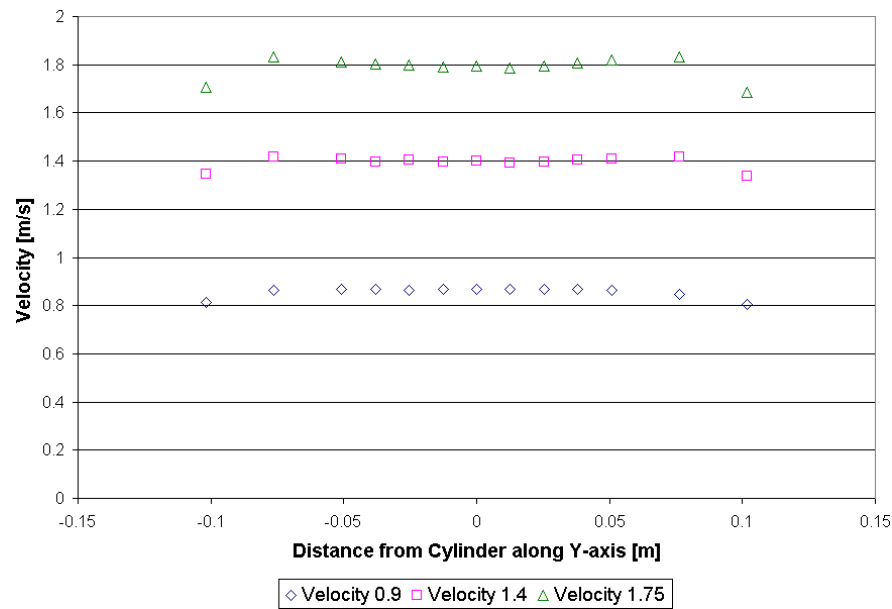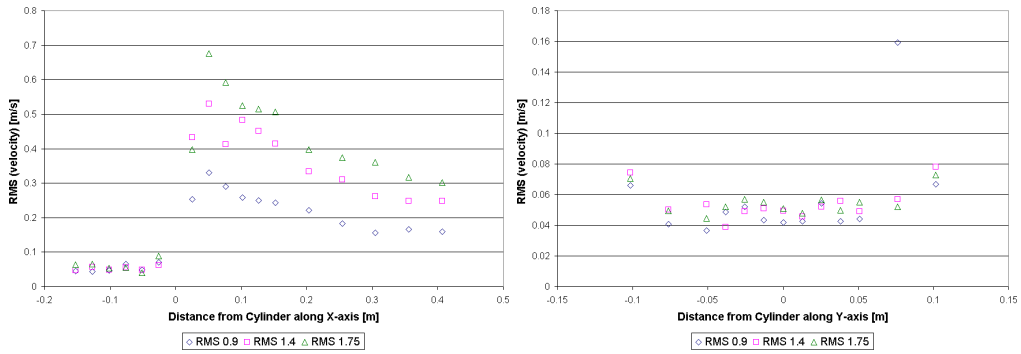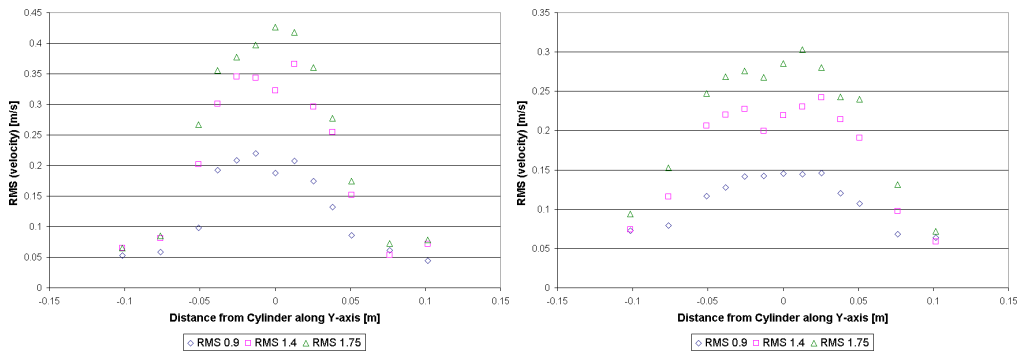

Figure 11: Axial velocity profile.

Figure 12: Velocity profile at 6 diameters upstream

(a) Axial.

(b) 6d upstream.

(c) 8d downstream.

(d) 8d downstream.

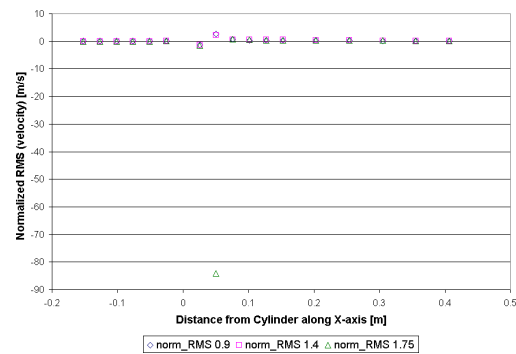Figure 13: RMS error of mean velocity.

Figure 14: Normalized RMS error.

C   Error Analysis

C.1   Sources of Error

Several types of errors in this experiment include random error, numerical error in approximated calculations, numerical error in sensor resolution, and theoretical assumptions made. Random error as well as numerical error were present in acquiring data from the pressure transducer and the LDV. Numerical error was due to approximating continuous integrals with the trapezoidal rule. Several assumptions such as irrotational flow and uniform flow were not completely true and contributed to error as well. Additionally, the motor had a limited resolution of ± 0.1 Hz, so the flow velocities were not exact. However, the for the purposes of this experiment, random error due to statistical variance was considered the most significant. These random errors were taken to be the RMS value of the pressure measurements and the velocity measurements. The error in velocity measurements in the turbulent section was overestimated by the RMS value, so the RMS value at the walls were used instead.

C.2   Drag Coefficient from Pressure Data

Propagation of the error in C_p, from pressure data, through the use of quadrature results in eqs. (21, 22, 23). Using eqs. (22, 23) in eq. (21) the value for C_p obtained at a velocity of 1.75 m/s is listed in eq. (24).

$$\delta C_{p,i} \;=\; \sqrt{\left(\frac{\partial C_{p,i}}{\partial q_\infty}\delta q_\infty\right)^2 + \left(\frac{\partial C_{p,i}}{\partial q_i}\delta q_i\right)^2} \tag{21}$$

$$\frac{\partial C_{p,i}}{\partial q_\infty} \;=\; -\frac{q_i}{q_i^2} \tag{22}$$

$$\frac{\partial C_{p,i}}{\partial q_i} \;=\; \frac{1}{q_\infty} \tag{23}$$

$$\delta C_p = 0.13 \tag{24}$$

Additional error is introduced in the calculation of C_D by use of the trapezoidal rule (eq. 7) to approximate the integral in eq. (6). The propagation of this error is listed in

eqs. (25, 26, 27). The error calculated at a velocity of 1.75 m/s are given in eqs. (28, 29). The remaining errors for C_D are listed in Table 4.

$$C_{D,i} = \sqrt{\left(\frac{\partial C_{D,i}}{\partial C_{p,i}}\delta C_{p,i}\right)^2 + \left(\frac{\partial C_{D,i}}{\partial C_{p,i+1}}\delta C_{p,i+1}\right)^2 + \left(\frac{\partial C_{D,i}}{\partial \theta_i}\delta\theta_i\right)^2 + \left(\frac{\partial C_{D,i}}{\partial \theta_{i+1}}\delta\theta_{i+1}\right)^2} \tag{25}$$

$$\delta C_{D,worst} = \sum_{i=1}^{N}\delta C_{D,i} \tag{26}$$

$$\delta C_{D,random} = \sqrt{\sum_{i=1}^{N}(\delta C_{D,i})^2} \tag{27}$$

$$\delta C_{D,worst} = 0.09 \tag{28}$$

$$\delta C_{D,random} = 0.03 \tag{29}$$

C.3 Drag Coefficient from LDV Data

The worst case and random errors in drag coefficient were propagated the same way as eqs. (26, 27) respectively. However, the individual component errors $C_{D,i}$ were propagated differently. From eq. (1), the partial derivatives (eqs. 31, 32) were taken and the error in C_D was expressed as eq. (30).

$$\delta C_{D,i} = \sqrt{\left(\frac{\partial C_{D,i}}{\partial F_{D,i}}\delta F_{D,i}\right)^2 + \left(\frac{\partial C_{D,i}}{\partial U_{1,\infty}}\delta U_{1,\infty}\right)^2} \tag{30}$$

$$\frac{\partial C_{D,i}}{\partial F_{D,i}} = \frac{1}{\frac{1}{2}\rho U_{1,\infty}^2 D} \tag{31}$$

$$\frac{\partial C_{D,i}}{\partial U_{1,\infty}} = -\frac{F_{D,i}}{\frac{1}{2}\rho U_{1,\infty}^3 D} \tag{32}$$

The error $\delta U_{1,\infty}$ was represented by the RMS value acquired from the LDV. However, the error $\delta F_{D,i}$ (eq. 33). was propagated in quadrature from its components (eqs. 34, 35, 36, 37). These expressions were obtained by taking the partial derivatives of the trapezoidal form of F_D (eq. 17).

$$
\delta F_{D,i} = \left[\left(\frac{\partial F_{D,i}}{\partial U_{1,\infty}} \delta U_{1,\infty} \right)^2 + \left(\frac{\partial F_{D,i}}{\partial U_{2,\infty}} \delta U_{2,\infty} \right)^2 + \right. \tag{33}
$$

$$
\left. \left(\frac{\partial F_{D,i}}{\partial U_2(y)_i} \delta U_2(y)_i \right)^2 + \left(\frac{\partial F_{D,i}}{\partial U_2(y)_{i+1}} \delta U_2(y)_{i+1} \right)^2 \right]^{1/2}
$$

$$
\frac{\partial F_{D,i}}{\partial U_{1,\infty}} = \rho U_{1,\infty} \left[\left[\frac{U_2(y)_i}{U_{2,\infty}} \left(1 - \frac{U_2(y)_i}{U_{2,\infty}} \right) \right] + \right. \tag{34}
$$

$$
\left. \left[\frac{U_2(y)_i}{U_{2,\infty}} \left(1 - \frac{U_2(y)_{i+1}}{U_{2,\infty}} \right) \right] \right] (y_i - y_{i+1})
$$

$$
\frac{\partial F_{D,i}}{\partial U_2(y)} = \frac{1}{2} \rho U_{1,\infty}^2 \left[\frac{1}{U_{2,\infty}} - 2 \frac{U_2(y)_i}{U_{2,\infty}^2} \right] (y_i - y_{i+1}) \tag{35}
$$

$$
\frac{\partial F_{D,i}}{\partial U_2(y)_{i+1}} = \frac{1}{2} \rho U_{1,\infty}^2 \left[\frac{1}{U_{2,\infty}} - 2 \frac{U_2(y)_{i+1}}{U_{2,\infty}^2} \right] (y_i - y_{i+1}) \tag{36}
$$

$$
\frac{\partial F_{D,i}}{\partial U_{2,\infty}} = \frac{1}{2} \rho U_{1,\infty}^2 \left[2 \frac{U_2(y)_i^2}{U_{2,\infty}^3} - \frac{U_2(y)_i}{U_{2,\infty}^2} + 2 \frac{U_2(y)_{i+1}^2}{U_{2,\infty}^3} - \frac{U_2(y)_{i+1}}{U_{2,\infty}^2} \right] (y_i - y_{i+1}) \tag{37}
$$

At a velocity of 1.75 m/s, the worst and random case errors were calculated at 8 and 16 diameters downstream. These results are shown in eqs. (38, 39, 40, 41). The error at all velocities were reported in Table 5.

$$
\delta C_{D,8d,worst} = 0.314 \tag{38}
$$

$$
\delta C_{D,8d,random} = 0.114 \tag{39}
$$

$$
\delta C_{D,16d,worst} = 0.503 \tag{40}
$$

$$
\delta C_{D,16d,random} = 0.166 \tag{41}
$$